BRAIN
ORIGINAL ARTICLE

Biallelic variants in *LIG3* cause a novel mitochondrial neurogastrointestinal encephalomyopathy

Elena Bonora,[1,†] Sanjiban Chakrabarty,[2,†] Georgios Kellaris,[3,†] Makiko Tsutsumi,[4,†] Francesca Bianco,[1,‡] Christian Bergamini,[5,‡] Farid Ullah,[3] Federica Isidori,[1] Irene Liparulo,[5] Chiara Diquigiovanni,[1] Luca Masin,[5] Nicola Rizzardi,[5] Mariapia Giuditta Cratere,[1,6] Elisa Boschetti,[1] Valentina Papa,[7] Alessandra Maresca,[8] Giovanna Cenacchi,[7] Rita Casadio,[9] Pierluigi Martelli,[9] Ivana Matera,[10] Isabella Ceccherini,[10] Romana Fato,[5] Giuseppe Raiola,[11] Serena Arrigo,[10] Sara Signa,[10] Angela Rita Sementa,[10] Mariasavina Severino,[10] Pasquale Striano,[10] Chiara Fiorillo,[10] Tsuyoshi Goto,[12] Shumpei Uchino,[13,14] Yoshinobu Oyazato,[15] Hisayoshi Nakamura,[16] Sushil K. Mishra,[17] Yu-Sheng Yeh,[12] Takema Kato,[4] Kandai Nozu,[18] Jantima Tanboon,[16] Ichiro Morioka,[19] Ichizo Nishino,[16] Tatsushi Toda,[20] Yu-ichi Goto,[21] Akira Ohtake,[22] Kenjiro Kosaki,[23] Yoshiki Yamaguchi,[24] Ikuya Nonaka,[16] Kazumoto Iijima,[18] Masakazu Mimaki,[13] Hiroki Kurahashi,[4] Anja Raams,[2] Alyson MacInnes,[25] Mariel Alders,[26] Marc Engelen,[27] Gabor Linthorst,[25] Tom de Koning,[28] Wilfred den Dunnen,[29] Gerard Dijkstra,[30] Karin van Spaendonck,[26] Dik C. van Gent,[2] Eleonora M. Aronica,[31] Paolo Picco,[10] Valerio Carelli,[7,8,§] Marco Seri,[1,§] Nicholas Katsanis,[3,§] Floor A. M. Duijkers,[26,§] Mariko Taniguchi-Ikeda[4,18,32,§] and Roberto De Giorgio[33,§]

[†,‡,§]These authors contributed equally to this work.

Abnormal gut motility is a feature of several mitochondrial encephalomyopathies, and mutations in genes such as *TYMP* and *POLG*, have been linked to these rare diseases. The human genome encodes three DNA ligases, of which only one, ligase III (*LIG3*), has a mitochondrial splice variant and is crucial for mitochondrial health.

We investigated the effect of reduced LIG3 activity and resulting mitochondrial dysfunction in seven patients from three independent families, who showed the common occurrence of gut dysmotility and neurological manifestations reminiscent of mitochondrial neurogastrointestinal encephalomyopathy. DNA from these patients was subjected to whole exome sequencing. In all patients, compound heterozygous variants in a new disease gene, *LIG3*, were identified. All variants were predicted to have a damaging effect on the protein. The *LIG3* gene encodes the only mitochondrial DNA (mtDNA) ligase and therefore plays a pivotal role in mtDNA repair and replication. *In vitro* assays in patient-derived cells showed a decrease in LIG3 protein levels and ligase activity. We demonstrated that the *LIG3* gene defects affect mtDNA maintenance, leading to mtDNA depletion without the accumulation of multiple deletions as observed in other mitochondrial disorders. This mitochondrial dysfunction is likely to cause the phenotypes observed in these patients. The most prominent and consistent clinical signs were severe gut dysmotility and neurological abnormalities, including leukoencephalopathy, epilepsy, migraine, stroke-like episodes, and neurogenic bladder. A decrease in the number of myenteric neurons, and increased fibrosis and elastin levels were

Received April 25, 2020. Revised November 13, 2020. Accepted December 9, 2020. Advance access publication April 15, 2021

the most prominent changes in the gut. Cytochrome *c* oxidase (COX) deficient fibres in skeletal muscle were also observed. Disruption of *lig3* in zebrafish reproduced the brain alterations and impaired gut transit *in vivo*.
In conclusion, we identified variants in the *LIG3* gene that result in a mitochondrial disease characterized by predominant gut dysmotility, encephalopathy, and neuromuscular abnormalities.

1 Department of Medical and Surgical Sciences, St. Orsola-Malpighi Hospital, University of Bologna, Bologna, 40138, Italy
2 Department of Molecular Genetics, Erasmus MC, Rotterdam, 3000 CA, The Netherlands
3 Center for Human Disease Modeling, Duke University, Durham, NC 27710, USA
4 Division of Molecular Genetics, Institute for Comprehensive Medical Science, Fujita Health University, Aichi, 470-1192, Japan
5 Department of Pharmacy and Biotechnology, University of Bologna, Bologna, 40126, Italy
6 Division of Genetics and Cell Biology, San Raffaele Scientific Institute, Milan, 20132, Italy
7 Department of Biomedical and Neuromotor Sciences, University of Bologna, Bologna, 40123, Italy
8 IRCCS Istituto delle Scienze Neurologiche di Bologna, Programma di Neurogenetica, Bologna, 40139, Italy
9 Biocomputing Group, Department of Biological, Geological, Environmental Sciences, University of Bologna, Bologna, 40126, Italy
10 IRCCS Istituto Giannina Gaslini, Genova, 16128, Italy
11 Department of Paediatrics, Pugliese-Ciaccio Hospital, Catanzaro, 88100, Italy
12 Laboratory of Molecular Function of Food, Division of Food Science and Biotechnology, Graduate School of Agriculture, Kyoto University, Uji, 611-0011, Japan
13 Department of Pediatrics, Teikyo University School of Medicine, Tokyo, 173-8605, Japan
14 Department of Pediatrics, Graduate School of Medicine, The University of Tokyo, Tokyo, 113-0033, Japan
15 Department of Pediatrics, Kakogawa Central City Hospital, Kakogawa, Hyogo, 675-8611, Japan
16 Department of Neuromuscular Research, National Institute of Neuroscience, National Center of Neurology and Psychiatry, Tokyo, 187-8502, Japan
17 Glycoscience Group, National University of Ireland, Galway, H91 CF50, Ireland
18 Department of Pediatrics, Kobe University Graduate School of Medicine, Hyogo, 650-0017, Japan
19 Department of Pediatrics and Child Health, Nihon University School of Medicine, Tokyo, 173-8610, Japan
20 Department of Neurology, Graduate School of Medicine, The University of Tokyo, Tokyo, 113-0033, Japan
21 Department of Mental Retardation and Birth Defect Research, National Institute of Neuroscience, National Center of Neurology and Psychiatry, Tokyo, 187-8502, Japan
22 Department of Pediatrics & Clinical Genomics, Faculty of Medicine, Saitama Medical University, Saitama, 350-0495, Japan
23 Center for Medical Genetics, Keio University School of Medicine, Tokyo, 160-8582, Japan
24 Laboratory of Pharmaceutical Physical Chemistry, Tohoku Medical and Pharmaceutical University, Miyagi, 981-8558, Japan
25 Department of Metabolic Diseases, Amsterdam UMC, University of Amsterdam, Amsterdam, 1100 DD, The Netherlands
26 Department of Clinical Genetics, Amsterdam UMC, University of Amsterdam, Amsterdam, 1100 DD, The Netherlands
27 Department of Neurology, Amsterdam UMC, University of Amsterdam, Amsterdam, 1100 DD, The Netherlands
28 Department of Metabolic Diseases, UMCG, Groningen, 9700 RB, The Netherlands
29 Department of Pathology, UMCG, Groningen, 9700 RB, The Netherlands
30 Department of Gastroenterology, UMCG, Groningen, 9700 RB, The Netherlands
31 Department of Pathology, Amsterdam UMC, University of Amsterdam, Amsterdam, 1100 DD, The Netherlands
32 Department of Clinical Genetics, Fujita Health University Hospital, Aichi, 470-1192, Japan
33 Department of Morphology, Surgery and Experimental Medicine, St. Anna Hospital, University of Ferrara, Ferrara, 44124, Italy

Correspondence to: Professor Roberto De Giorgio
Department of Morphology, Surgery and Experimental Medicine, University of Ferrara, 44124 Ferrara, Italy
E-mail: roberto.degiorgio@unife.it

Correspondence may also be addressed to: Dr Floor A. Duikers
Department of Clinical Genetics. Amsterdam University Medical Centers, University of Amsterdam
1105 AZ, Amsterdam, The Netherlands
E-mail: f.a.duijkers@amsterdamumc.nl

Associate professor Mariko Taniguchi-Ikeda
Department of Clinical Genetics, Fujita Health University Hospital, 1-98, Dengakugakubo Kutsukake-cho Toyoake, Aichi 470-1192, Japan
E-mail: mtani@fujita-hu.ac.jp or taniguchi_mariko@me.com

Keywords: mtDNA repair; mtDNA replication; *LIG3*; MNGIE; CIPO

Abbreviations: CIPO = chronic intestinal pseudo-obstruction; dpf = days-post-fertilization; MNGIE = mitochondrial neurogastrointestinal encephalomyopathy; MO = morpholino; USC = urothelial sediment cell; WES = whole exome sequencing

Introduction

The human genome encodes three DNA ligases (I, III and IV). All DNA ligases are expressed in the nucleus, but only ligase III (*LIG3*) has a mitochondrial splice variant. Nuclear LIG3 interacts with X-ray repair cross-complementing protein 1 (XRCC1) for DNA maintenance by base excision repair, but other nuclear ligases can compensate for defects in the *LIG3* gene, which encodes the LIG3 protein.[1–5] However, LIG3 is crucial in mitochondria, as it is the only ligase responsible for mitochondrial DNA (mtDNA) replication and maintenance, working along with mtDNA polymerase gamma (POLG) and other mtDNA replisome factors.[6] The lethality of a *LIG3* null mutation can be alleviated by targeting another DNA ligase to mitochondria, whereas overexpression of the LIG3 protein appears to increase the resistance to oxidative damage in mitochondria.[7] Therefore, reduced LIG3 activity is expected to affect mitochondrial health and would lead to diseases resulting from mitochondrial dysfunction.

A key clinical feature of several mitochondrial diseases is severely abnormal gut motility, such as in patients with chronic intestinal pseudo-obstruction (CIPO). This is an impairment of gut propulsion, mimicking a mechanical obstruction without detectable anatomical causes.[8–10] Mitochondrial encephalomyopathies may also be characterized by prevalent leukoencephalopathy caused by mitochondrial dysfunction.[6] Mitochondrial neurogastrointestinal encephalopathy (MNGIE), the 'tip of the ice-berg' of such rare diseases, is caused by mutations in the *TYMP* gene, which encodes thymidine phosphorylase.[11] Similar phenotypes are also caused by mutations in *POLG*, or mutations in the mtDNA itself, as observed in patients with mitochondrial encephalomyopathy with lactic acidosis and stroke-like episodes (MELAS).[12]

We here report a novel mitochondrial gastrointestinal encephalomyopathy caused by biallelic variants in *LIG3*,[1,3,13,14] leading to a syndrome predominantly characterized by severe gut dysmotility (i.e. CIPO) and encephalomyopathy.

Patients and methods

In the present study, analyses of the patients were performed in three different institutes, which led to some differences in the methods used per family, as detailed below.

Ethical approval

Data from patients and controls were handled in accordance with the local ethics committees (St. Orsola Hospital Ethics Committee; Institutional Review Board of Kobe University School of Medicine and Medical Ethical Board of Amsterdam University) and analyses were performed after obtaining written informed consent from the patients or patients' parents, according to the Declaration of Helsinki.

Next-generation sequencing analysis

Families were recruited from different institutions as follows: Italy, Family 1, Patients 1-1, 1-2, and 1-3; The Netherlands, Family 2, Patients 2-1 and 2-2; and Japan, Family 3, Patients 3-1 and 3-2. Details of patients are provided in the Supplementary material.

Sample collection and immunohistochemistry

Muscle, gut, skin and urothelial sediment cells (USCs) were collected and histologically analysed as described in the Supplementary material. Procedures for western blot analyses are also provided in the Supplementary material.

Immunofluorescence: Family 1

Immunofluorescence analysis was performed as described in the Supplementary material. The following primary antibodies were used: rabbit anti-LIG3 (26583-1-AP; 1:50, ProteinTech). Secondary antibodies used were the following: Alexa Fluor® 488 goat anti-rabbit IgG, Alexa Fluor® 555 goat anti-rabbit (all from Abcam; 1:800).

Analysis of mtDNA content by real-time quantitative PCR

Family 1

Total DNA was extracted from fibroblasts using the Qiagen Mini kit and from muscle biopsies by standard phenol-chloroform extraction. Real-time quantitative PCR was used to assess mtDNA content according to previously validated methods.[15]

Family 2

The mtDNA/nuclear DNA (nDNA) ratio was measured in duplicate on freshly obtained muscle tissue in a diagnostic setting (Radboud UMC Laboratory, The Netherlands) and compared to age-matched controls (above the age of 21 years) from reports in the literature.[16]

Family 3

Total DNA was extracted from fibroblasts or myoblasts using DNeasy Blood and Tissue Kit (Qiagen). The Human mtDNA Monitoring Primer Set (Takara) was used for amplification of mtDNA and nDNA. Real-time PCR was performed using SYBR Premix Ex Taq II (Takara) and 7300 Real-Time PCR System (Thermo Fisher) according to previously published protocols.[17,18]

DNA ligase assay: Patient 2-1

Mitochondrial protein extracts were prepared from primary fibroblasts as previously described.[19] Ligation of linearized pUC18 plasmid using mitochondrial extracts was performed as previously reported.[19] Briefly, PstI-linearized pUC18 was incubated at 16°C for 16 h with mitochondrial extracts from control and mutant samples.

Plasmid DNA was subsequently deproteinized, purified and separated on 1.2% analytical agarose gels. Reactions were supplemented by the addition of ATP; T4 DNA ligase (New England Biolabs) was used as a positive control. Each ligation assay was performed twice.

Quantitative PCR-based analysis of mtDNA repair activity

Wild-type and *LIG3*-mutant fibroblasts (10^6) from Patient 2-1 were seeded in 6-cm dishes 16–18 h prior to the experiments. Cells were washed once with Ham's F-10 medium without supplements, and the conditioned medium was used subsequently. Cells were exposed to 200 μM H_2O_2 for 15 min and harvested immediately or cultured with conditioned medium for 6 h. High-molecular weight genomic DNA was extracted from untreated or H_2O_2-treated wild-type and *LIG3*-mutant cell lines using Wizard® SV Genomic DNA Purification System (Promega). The quantitative PCR reaction was performed with the LongAmp® Taq PCR kit (New England Biolabs) as follows: 15 ng total DNA was added to a reaction mix of 50 μl with 100 ng/μl bovine serum albumin, 200 μM dNTPs each, 1–3 mM $MgO(Ac)_2$, and 20 pmol each of the two primers. PCR was performed with primer pairs to amplify an 8.9-kb fragment of mtDNA (long), and in a separate reaction to amplify a 221-bp fragment of mtDNA (short), to calculate mtDNA damage and copy number in untreated and H_2O_2-treated samples, respectively.[17] The primer sequences used were as previously described.[17] PCR products for both long and short mitochondria amplicons were quantified using the PicoGreen™ dsDNA quantification assay (Thermo Fisher). Fluorescent values obtained from the short PCR products of each sample were used to normalize the results from the long PCR products. These values were used to estimate the average number of lesions per 10 kb mitochondrial genome using a Poisson distribution.[17] Relative amplification was calculated by comparing treated samples with untreated samples for both wild-type and mutant cells and the unpaired *t*-test was performed for statistical analysis.

Ethidium bromide treatment: Patient 3-2

Fibroblasts were cultured in the presence of 50 ng/ml ethidium bromide (EtBr), 1 mM pyruvate, and 50 μg/ml uridine for 9 days followed by culturing without EtBr for 7 days. Subcultures were performed every 2 to 3 days to keep the confluency of the cells between 30% and 80%.

Mitochondrial oxygen consumption

Patient 1-1

To measure mitochondrial oxygen consumption 1.5×10^6 cells for each cell type (wild-type and Patient 1-1-derived fibroblasts) were harvested, washed in PBS, resuspended in complete medium and assayed for oxygen consumption at 37°C using a thermostatically regulated oxygraph chamber (Instech Mod.203). Basal respiration was measured in Dulbecco's modified Eagle medium and compared with data obtained after the injection of oligomycin (1 μM) and carbonyl cyanide 4-(trifluoromethoxy) phenylhydrazone (FCCP) (1–6 μM). Antimycin A (5 μM) was added at the end of the experiments to completely block the mitochondrial respiration.[20] Respiratory rates were expressed in nmol O_2/min/mg of total protein, which was determined by the Lowry assay.

Patient 3-2

In USCs, basal and maximal oxygen consumption rates (OCR) were analysed using Seahorse Bioscience XF-24 extracellular flux bioanalyzer (Agilent) and Seahorse XF Cell Mito Stress Test. USCs were seeded onto XF 24-well microplates in growth medium at 1.5×10^5/well ($n = 5$). The next day, growth medium was replaced with assay medium supplemented with glucose, pyruvate and L-glutamine, and the pH was adjusted to 7.4. Cells were equilibrated prior to Mito Stress testing in the analysis medium for 30 min at 37°C in a CO_2-free incubator. ATP-linked respiration was determined by oligomycin (1 μM) and maximal respiration was induced using FCCP (1 μM). Nonmitochondrial respiration was determined after injection of rotenone and antimycin A (1 μM each). Data were analysed using XF Cell Mito Stress Test Report Generator. After assay completion, cells were rinsed with PBS and frozen. After thawing, double stranded DNA of each well was measured using DNA Quantity kit (Cosmo BIO) using a microplate reader.

ATP determination: Patient 1-1

Nucleotides were extracted and detected using a Kinetex C18 column (250 × 4.6 mm, 100 Å, 5 μm; Phenomenex) with a two pump Agilent 1100 series system (Agilent).[21] Absorbance (260 nm) was monitored with a photodiode array detector (Agilent 1100 series system). Nucleotide peaks were identified by comparison and coelution with known standards and quantification by peak area measurement compared with standard curves.

Zebrafish husbandry

Embryos were obtained by natural mating of wild-type adults (TU/AB strain, Aquatica BioTech). Adults were maintained on a 14-h/10-h day/night cycle. Larvae were nurtured in embryo media (0.3 g/l NaCl, 75 mg/l $CaSO_4$, 37.5 mg/l $NaHCO_3$ and 0.003% methylene blue) at 28°C until phenotypic analysis at 3 days post fertilization (dpf), 5 dpf and 8 dpf, respectively. All zebrafish studies were approved by the Duke University Institutional Animal Care and Use Committee.

Gene suppression and complementation in zebrafish embryos

A splice-blocking morpholino (MO) was designed to target the *Danio rerio lig3* exon 11 splice donor (e11i11) and was synthesized by Gene Tools LLC. To identify the optimal dose for *in vivo* complementation, a dose curve was generated by injecting 2, 4 and 6 ng (1 nl MO per embryo; one- to four-cell stage) into TU/AB embryos. Total RNA was extracted from 1 dpf embryos (15–20 per condition) using TRIzol® (Thermo Fisher) and was reverse transcribed using the SuperScript® III Reverse Transcriptase kit (Thermo Fisher). We used cDNA as the template for RT-PCR with primers flanking the *lig3* MO target site. PCR products were purified with QIAquick gel extraction kit (Qiagen) and cloned in TOPO-TA cloning vector (Thermo Fisher). Plasmids were purified and Sanger sequenced according to standard protocols. For rescue experiments, wild-type human *LIG3* open reading frame (Ultimate ORF collection; Clone ID: IOH40893) was subcloned into the pCS2+ vector by LR Clonase II®-mediated recombination (Thermo Fisher). To produce constructs containing the sequences of patient-associated variants, site-directed mutagenesis was performed.[22] Constructs were linearized with *NotI*, and the resulting template was transcribed with the mMessage mMachine® SP6 transcription kit (Thermo Fisher). Unless otherwise noted, 6 ng *lig3* MO was used either alone or in combination with 200 pg *LIG3* mRNA for *in vivo* complementation studies.

CRISPR/Cas9 genome editing of zebrafish embryos

Guide (g) RNAs targeting the *lig3*-coding region were designed with CHOPCHOP. A GeneArt precision gRNA synthesis kit (Thermo Fisher) was used to *in vitro* transcribe gRNAs, followed by injection of 1 nl of injection cocktail containing 100 pg/nl gRNA and 200 pg/nl Cas9 protein (PNA Bio) directly into the cell of TU/AB embryos (one-

cell stage). Heteroduplex assays were used to determine targeting efficiency in founder (F0) mutants.[23,24] Genomic DNA was extracted from 2 dpf embryos. The region flanking the gRNA target site was amplified by PCR; PCR products were denatured (95°C for 2 min), reannealed (–2°C/s to 85°C and –0.1°C to 25°C), separated on a 15% TBE 1.0-mm polyacrylamide gel, stained with EtBr and imaged using the Chemi-Doc system (Bio-Rad). To estimate the percentage of mosaicism of *lig3* F0 mutants ($n = 5$), PCR products were gel-purified with QIAquick Gel extraction kit (Qiagen), cloned into the TOPO-TA vector (Thermo Fisher) and plasmids were isolated from individual colonies ($n = 10$–12 colonies/embryo) and Sanger sequenced according to standard procedures.

Phenotypic analysis of zebrafish larvae

Whole-mount immunostaining with anti-acetylated tubulin (T7451, Sigma-Aldrich) and anti-HuC/D (A-21271, Thermo Fisher) antibodies was performed to analyse the brain and enteric neurons along the gastrointestinal tract, respectively. Smooth muscle morphology of the gastrointestinal tract was assessed using the anti-phospho-myosin light chain 2 antibody (Ser19; 9970, CST). To quantify neurons in the cerebellar area, whole-mount acetylated tubulin immunostaining was performed.[22,25] Dorsal images were acquired manually with an AxioZoomV.16 microscope (Zeiss) and Axiocam 503 monochromatic camera (Zeiss). Cerebellar structures of interest were measured using ImageJ software. Total cerebellar area was measured blindly by two experts on acetylated tubulin-stained larvae by outlining the structures with a fluorescent signal. Quantitative evaluation of enteric neurons was performed via HuC/D staining in injected embryos at 5 dpf. For phospho-myosin staining, injected embryos were analysed at 8 dpf. Fluorescent cell counts were performed with ImageJ software. To assess peristalsis of the zebrafish gut, embryos at 8 dpf were anaesthetized using 1× tricaine embryo media. Gastrointestinal motility was recorded with 2-min time lapse videos.

Statistical analysis

Chi-squared (χ^2), ANOVA and two-tailed parametric *t*-tests were performed as reported in the corresponding 'Results' sections and figure legends, using GraphPad Prism software v.7.00 (GraphPad). *P*-values < 0.05 were considered to indicate a statistically significant difference between two groups. For statistical analysis of cerebellum measurements in zebrafish, a non-parametric one-way ANOVA followed by the Tukey multiple comparison test was performed. For the gut peristalsis assay, the χ^2 test was used to perform pairwise statistical comparisons across experimental conditions.

The analysis of mtDNA deletions by droplet digital PCR, RNA extraction and transcript analysis, ultrastructural analysis, mitochondrial network analysis, reactive oxygen species quantification, and measurement of transmembrane potential are described in the Supplementary material.

Data availability

The authors confirm that the data supporting the findings of this study are available within the article and its Supplementary material.

Results

Clinical features of the patients

In seven affected individuals from three separate families compound heterozygous variants in the *LIG3* gene were identified by whole exome sequencing (WES) (Fig. 1A–C). These patients showed a largely overlapping phenotype and an overview of their clinical features is presented in Table 1. The clinical histories of each patient can be found in the Supplementary material. The clinical features of these patients for many aspects resembled the mitochondrial disease MNGIE. Severe dysmotility of the gut was present in all patients and most patients fulfilled the diagnostic criteria for CIPO.[8–10,26] Brain MRI of all patients showed leukoencephalopathy and/or progressive cortical atrophy, whereas cerebellar atrophy was observed only in patients from Family 3 (Fig. 1D–F). In addition to the MNGIE-like features, all patients had other neurological features including epilepsy, stroke-like episodes, migraine and developmental delay, reminiscent of MELAS. Further clinical manifestations included neurogenic bladder and macular degeneration, which were present in most patients. Hearing loss was only observed in one patient (Table 1). Increased lactate/pyruvate ratio in the CSF was found in the patients of Family 3. Although the clinical phenotype was quite consistent across the three families, the age of onset and disease severity differed considerably ranging from paediatric severe disease with premature death to adult cases. In particular, the two patients of Family 3 manifested as infants with severe gut dysmotility, severe developmental delay and epilepsy, interpreted as West syndrome.[27] One of the two children in this family died at the age of 2 years. Conversely, the disease onset occurred much later in the three patients from Family 1 (between the ages of 9 and 10 years), with a rapid disease progression. The presentation in Family 2 was even later, with some features detectable at paediatric age, but the most severe manifestations only occurring at adult age with a slower disease progression compared with the other two families.

Evidence of mitochondrial dysfunction in patient tissue

Skeletal muscle biopsies of patients from all three families (Patients 1-1, 2-2 and 3-2) showed alterations that are observed in patients with mitochondrial myopathies, e.g. succinate dehydrogenase (SDH) hyper-reactivity, reduced cytochrome *c* oxidase (COX)-staining (Supplementary Fig. 1A–C) and altered myofibre structure (Patient 3-2) on electron microscopy (Supplementary Fig. 1D). Nevertheless, these muscle alterations were variable/subtle, as compared with the severe clinical phenotype observed in the gut and CNS of the patients.

Identification of *LIG3* mutations

The recurrent phenotype of CIPO and neuromuscular involvement in all sibs, along with unaffected parents, suggested a recessive disorder, with a possible mitochondrial aetiology. In all three families we identified compound heterozygous variants in *LIG3*, shared by the corresponding affected sibs and inherited from the corresponding heterozygous healthy parents (Fig. 2A and Supplementary Fig. 2A–C). The variants in Family 1 (p.K537N and p.G964R missense variants) were not present in public databases (Database of Single Nucleotide Polymorphisms, dbSNP; Genome Aggregation Consortium, gnomAD; ClinVar; 1000Genomes) or in an inhouse database (650 Italian exomes). In Family 2 the missense variant p.C999Y was novel and the premature stop codon p.R267Ter was present in dbSNP with a very low minor allele frequency (MAF) (Supplementary Table 1). In Family 3 we identified the missense variant p.P609L and the premature stop codon p.R811Ter. Both variants were present in dbSNP and gnomAD with a very low MAF (Supplementary Table 1). No deleterious variants in other genes compatible with a recessive or *de novo* inheritance were detected. All variants mapped to the conserved LIG3

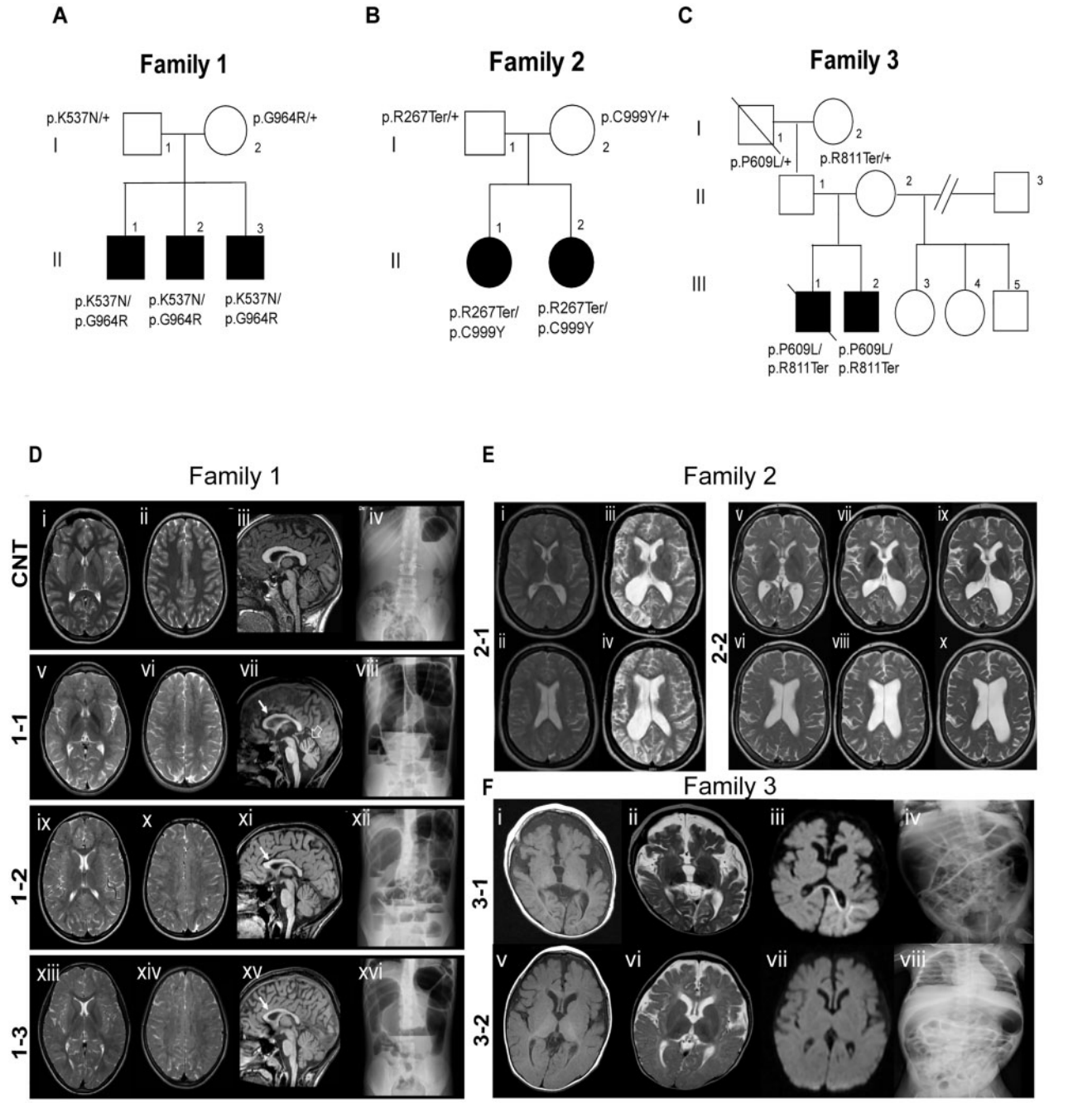

Figure 1 Identification of *LIG3* mutations. (**A**–**C**) Pedigrees of the three families with *LIG3* mutations. Filled and open symbols denote affected and healthy individuals, respectively; diagonal bars indicate deceased members. (**A**) Family 1: inheritance of paternal p.K537N and maternal p.G964R variants in the three affected brothers. (**B**) Family 2: inheritance of paternal p.R267Ter and maternal p.C999Y variants in the two affected sisters. (**C**) Family 3: inheritance of paternal p.P609L and maternal p.R811Ter variants in the two affected brothers. (**D**) Brain MRI and abdominal X-ray images of the patients in Family 1. (**ii**) Axial T_2-weighted, and (**iii**) sagittal T_1-weighted images of a control subject (CNT) demonstrating normal supratentorial white matter, corpus callosum and cerebellar vermis. Corresponding images for Patients 1-1 (**v**–**vii**), 1-2 (**ix**–**xi**) and 1-3 (**xiii**–**xv**) demonstrate leukoencephalopathy (involving periventricular and subcortical white matter, corpus callosum and internal capsules) characterized by diffuse but irregular T_2 hyperintensities with a peculiar 'leopard-skin' pattern due to the sparing of small white matter islets. Arrows (**vii**, **xi** and **xv**) indicate mild callosal hypoplasia. Patient 1-1 shows additional signs of cerebellar atrophy (**vii**, open arrow). (**viii**–**xvi**) Abdominal X-ray images displaying bowel dilatation with air-fluid levels compared with the control subject. (**E**) Brain MRI of the patients of Family 2. Axial T_2-weighted images of Patients 2-1 (*left*) and 2-2 (*right*) at different time points (**i**, t = 0 years and **iii**, t = +3 years; **v** and **vi**, t = 0; **vii** and **viii**, t = +2 years, **ix** and **x**, t = +4 years). In Patient 2-1 there is diffuse hyperintensity of the entire cerebral white matter. After several stroke-like episodes, progressive atrophy with asymmetrical '*ex vacuo*' dilatation of the ventricular system was noted. Patient 2-2 displays a similar pattern and evolution over time. (**F**) Brain MRI and abdominal X-ray images of patients in Family 3. In Patient 3-1 axial (**i**) T_1-weighted, (**ii**) T_2-weighted and (**iii**) diffusion-weighted images demonstrate brain atrophy and restricted diffusion in the left temporo-occipital, corticosubcortical regions extending to the corpus callosum. In Patient 3-2, brain MRI demonstrates generalized brain atrophy (**v**–**vii**). Abdominal X-ray images show marked bowel distension (**iv** and **viii**).

Table 1 Clinical features of the affected sibs with LIG3 compound heterozygous variants

	Patient 1-1	Patient 1-2	Patient 1-3	Patient 2-1	Patient 2-2	Patient 3-1	Patient 3-2
Current age, years	17	13	11	40	39	2 (deceased)	4
Age of onset, years	9	10	10	18	18	1	2
GI symptoms and surgery	Subacute and/or recurrent episodes of intestinal obstruction without an occluding lesion, malnutrition (parenteral nutrition), diarrhoea, ileostomy (at 16 years)	Subacute and/or recurrent episodes of intestinal obstruction without an occluding lesion, malnutrition (parenteral nutrition), abdominal distension and constipation, ileostomy (at 11 years)	Subacute and/or recurrent episodes of intestinal obstruction without an occluding lesion, diarrhoea/constipation, ileostomy (at 10 years)	Chronic intestinal pseudo-obstruction (18 years), TPN (from 33 years), enlarged liver, cholecystolithiasis	Chronic intestinal pseudo-obstruction (at 18 years), TPN (at 37 years).	Severe abdominal distension, hepatomegaly, NG tube (at 1 month)	Severe abdominal distension, hepatomegaly, NG tube (at 1 month), IVH (at 2 years)
Brain imaging	Diffuse leukoencephalopathy, cerebellar atrophy	Diffuse leukoencephalopathy, thin corpus callosum	Diffuse leukoencephalopathy	After a stroke-like event at 33 years, increasing degree of atrophy and gliosis over time, most prominent in parietal-occipital right hemisphere	Progressive diffuse leukoencephalopathy after stroke-like episodes	Leukoencephalopathy, cerebellar atrophy	Leukoencephalopathy, cerebellar atrophy
Neurological signs	Pyramidal signs, mild ataxia, dysmetria	Pyramidal signs	Pyramidal signs	Unilateral neglect and cognitive deterioration/decline after stroke-like episode at 33 years	Nystagmus and diminished feeling in the legs and cognitive deterioration at 36 years	Involuntary movements, jerks	Involuntary movements, jerks
Headache	Yes, complicated with motor deficits	Yes, complicated with motor deficits	Yes, complicated with motor deficits	Yes, migraine with aura, starting from teenage years	Yes, migraine with aura, starting from paediatric years	N/A	N/A
Psychiatric features	Repetitive pattern of behaviours and interests	Repetitive pattern of behaviours	None	None	None	N/A	N/A
Urogenital abnormalities	Neurogenic bladder, right mild pyelectasia	Neurogenic bladder	None	Possible voiding dysfunction, frequent retention bladder	Unilateral duplicated collecting system, frequent retention bladder	N/A	Neurogenic bladder
Additional features	Recurrent arthralgias, stomatitis, macular degeneration	Macular degeneration	None	Macular degeneration	Macular degeneration, frequent infections (recent years)	Apnoea, recurrent infections, pneumonia	Cataracts, hearing loss, dysphagia

GI = gastrointestinal; IVH = intravenous hydration; N/A = not assessed; NG = nasogastric; TPN = total parenteral nutrition.

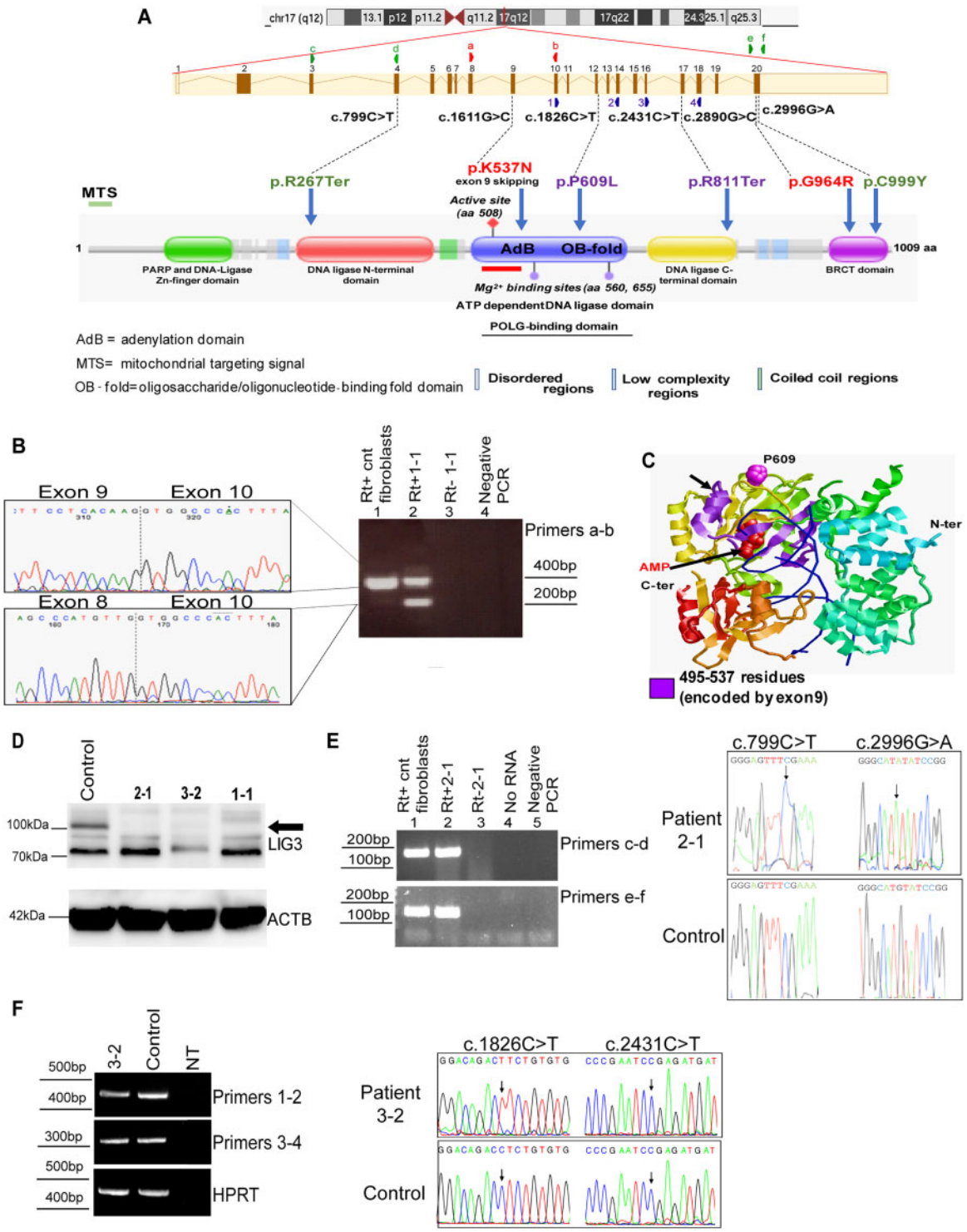

Figure 2 Identification of the molecular defects of *LIG3*. (**A**) Mutations mapped on the Pfam database (https://pfam.xfam.org/) domains of LIG3 [mitochondrial transport signal (MTS), ATP-binding domain, POLG and XRCC1-binding sites]. Variants in Family 1 are indicated in red, variants in Family 2 are indicated in green, and variants in Family 3 are indicated in violet. Arrowheads indicate the primer pairs used for subsequent RT-PCR analysis. aa = amino acids. (**B**) Splicing alteration induced by the p.K537N variant. Control fibroblasts (lane 1, cnt) show a band of the expected size for the transcript containing exon 9. Fibroblasts from Patient 1-1 (lane 2) show two bands: the higher band corresponds to the transcript with exon 9, and the lower band corresponds to a transcript without exon 9, as shown by the corresponding electropherograms. A cropped image of the gel electrophoresis is reported, without the marker lane (relevant sizes indicated; bp = base pairs). Lane 3: no RT = RT-PCR carried out without reverse transcriptase on Patient 1-1 mRNA; lane 4: negative control of RT-PCR (no template). (**C**) Structure of the ligase domain of human LIG3 (residues 257-833) in complex with DNA and AMP. The region encoded by exon 9 is in violet. The position p.P609 is represented in pink. (**D**) LIG3 western blot analysis in total cell lysates derived from human control and patient fibroblasts, showing a severely decreased LIG3 protein levels (black arrow) in patient fibroblasts compared with controls. ACTB = beta-actin loading control. Immunoblotting for LIG3 and for ACTB (endogenous control) proteins were performed on the same blot. Cropped images are reported. (**E**) *LIG3* transcript analysis in Patient 2-1 and control cDNAs. *Left*: Agarose gel electrophoresis image of the RT-PCR products. Cropped images of gel electrophoresis are reported, without the marker lane (relevant sizes indicated). *Right*: Sanger sequencing

(continued)

domains[28,29] and *in silico* analyses predicted their pathogenicity (Fig. 2A, Supplementary Fig. 2D and Supplementary Tables 1 and 2).[30,31] No causative point mutations or deletions in mtDNA were identified in Patients 1-1, 2-2 and 3-2.

LIG3 mRNA and protein analysis

Detailed analyses on the consequences of the *LIG3* mutations were conducted using primary skin fibroblasts derived from Patients 1-1, 2-1 and 3-2. The missense p.K537N variant identified in Family 1, mapping to the most 3′ nucleotide of exon 9, was predicted to alter splice-site recognition (Human Splicing Finder v3.0, HSF; Supplementary Fig. 3A). RT-PCR with the primers in exon 8 and exon 10 showed only one band of the expected size for exon 9 inclusion in control cDNA, but the cDNA from patient cells also gave rise to a shorter transcript lacking exon 9 (Fig. 2B). Exon 9 skipping results in a protein lacking 52 amino acids (495–537 in-frame deletion) in the conserved adenylation-nucleotidyltransferase (NTase) domain of the ATP- and POLG-binding regions (Fig. 2C).[13,14,28] Exon skipping in this mutant protein results in the loss of ∼5 kDa of the LIG3 protein. However, we detected a severe reduction in the total amount of LIG3 protein without the appearance of a shorter LIG3 species on western blot analysis of control and patient fibroblast lysates (Fig. 2D) (a severe reduction in expression is also shown in Supplementary Fig. 3B–D). Concordantly, transient transfection of the cDNA encoding for human *LIG3* carrying the exon 9 deletion in HEK293 cells did not show any band smaller than that of the wild-type LIG3 protein (Supplementary Fig. 3E), suggesting that the protein is early degraded. Although in Patient 1-1 fibroblasts the exon 9 variant gave rise to exon skipping, we also evaluated its potential effect as missense change p.K537N in transient transfection of HEK293: the protein product was present (Supplementary Fig. 3F), but the co-immunoprecipitation assay using an antibody against LIG3, followed by western blotting for POLG, showed a very low affinity for POLG compared to wild-type LIG3 (Supplementary Fig. 3G). Based on western blot results in fibroblasts, we assumed that, in the Patient 1-1 fibroblasts, only the other human LIG3 allele (p.G964R) was expressed at the protein level and that this amino acid change caused reduced stability. In line with these observations, transient transfection of the cDNA encoding for human LIG3 with the missense change p.G964R in HEK293 revealed that LIG3 expression was comparable to that of the empty vector, at difference with the HEK293 cells transfected with wild-type LIG3 (Supplementary Fig. 3F). Molecular modelling showed that p.G964 interacts with p.R558 of murine XRCC1 (a residue conserved between human and murine proteins). The LIG3 variant p.G964R was predicted to hamper the interaction between LIG3 and XRCC1 because of the close proximity (0.44 nm) of two positively charged amino acids in the interacting site (p.R558 in XRCC1 and mutated p.R964; Supplementary Fig. 3H). This impairment prevented LIG3 translocation into the nucleus (Supplementary Fig. 3I).[1–3]

The compound heterozygous mutations in Family 2 (p.R267Ter and p.C999Y) were also analysed. RT-PCR on Patient 2-1 fibroblasts and controls showed that the c.799C>T allele (p.R267Ter variant) was not expressed, and only the c.2996G>A allele (p.C999Y variant) was present in the final transcript of the patient's fibroblasts (Fig. 2E), suggesting that mRNA carrying the c.799C>T variant (premature stop codon p.R267Ter) was degraded by nonsense-mediated decay. Transient transfection of HEK293 cells with the plasmid encoding the LIG3 p.C999Y variant did not show an increase in expression, compared to cells transfected with the empty vector, as seen for the vector with wild-type LIG3 (Supplementary Fig. 3F). Molecular modelling showed that the variant p.C999Y is predicted to severely destabilize LIG3 structure (ΔΔG = –2.02 kcal/mol; Supplementary Fig. 3H).[28–31] Western blot analysis in patient's fibroblasts indeed resulted in a marked decrease in LIG3 protein levels (Fig. 2D and Supplementary Fig. 3C).

The p.R811Ter variant in Family 3 was not expressed and only the c.1826C>T allele (p.P609L variant) was present in the final transcript (Fig. 2F), suggesting that mRNA carrying the c.2431C>T variant (premature stop codon p.R811Ter) was degraded by nonsense-mediated decay, as shown for the premature stop-codon found in patients of Family 2. The p.P609L variant, mapping to the end of an alpha-helix in the ATP-binding domain, was predicted to destabilize the protein (ΔΔG = –0.74 kcal/mol; Fig. 2C).[30,31]

Compared to controls, fibroblasts from Patient 3-2 showed very low amounts of LIG3 protein (Fig. 2D and Supplementary Fig. 3D), in agreement with the transient transfection of the construct carrying the p.P609L variant in HEK293 cells (Supplementary Fig. 3F). We also investigated whether protein instability could be rescued by the proteasome inhibitor MG132 which, however, evoked only a marginal increase of LIG3 levels in mutant cells (Supplementary Fig. 3D).

LIG3 mutations result in impaired ligase activity and mtDNA depletion

As LIG3 is the only mtDNA ligase, we investigated whether the ligase activity of mitochondrial extracts from patient cells was affected. The mitochondrial extracts from control and Patient 2-1 fibroblasts were incubated with linearized plasmid DNA (Fig. 3A). Indeed, mutant extracts were unable to religate the linearized plasmid DNA, whereas mitochondrial extracts from control cells showed clear ligation activity. Subsequently, the mtDNA ligation and repair capacity was analysed in control and patient fibroblasts, according to Furda *et al.*[17] Control and mutant cells were exposed to oxidative stress (H_2O_2 for 15 min) and then allowed to repair the DNA damage for 6 h (Fig. 3B). Normal fibroblasts showed a reduced amount of PCR amplification product directly after the H_2O_2 exposure and a significant recovery after 6 h ($P < 0.05$; Fig. 3B). However, mutant cells showed little or no recovery of intact mtDNA, consistent with a severe defect in mtDNA repair (Fig. 3B).

We also investigated whether mtDNA replication was affected. The replication capacity of mtDNA after EtBr treatment was impaired in fibroblasts from Patient 3-2. Control and patient cells lost their mtDNA content at a similar rate and after 9 days of EtBr treatment all cells contained only low levels of mtDNA (controls between 0.5% and 1.2%; patient 0.9% of the starting level). However, the controls showed a clear increase in mtDNA content 6 days after withdrawal of EtBr, whereas this recovery was not observed in the patient samples. This experiment demonstrates that the patient cells have a clearly decreased capacity of mtDNA

Figure 2 Continued
analysis of the products of RT-PCR with primers c–d and primers e–f. Arrows indicate the c.799C>T and c.2996G>A variants in *LIG3* transcript. The electropherogram shows that only the c.2996G>A (p.C999Y) variant is present in the *LIG3* transcript of the patient, and not the c.799C>T (p.R267Ter) variant. (**F**) *LIG3* transcript analysis in Patient 3-2 and control cDNAs. *Left*: Agarose gel electrophoresis image of the RT-PCR products. HPRT = internal control. Cropped images of gel electrophoresis are reported, without the marker lane (relevant sizes indicated). *Right*: Sanger sequencing analysis of the products of RT-PCR with primers 1–2 and primers 3–4. Arrows indicate the c.1826C>T and c.2431C>T variants in *LIG3* transcript. The electropherogram shows that only the c.1826C>T (p.P609L) variant is present in the *LIG3* transcript of the patient, and not the c.2431C>T (p.R811Ter) variant.

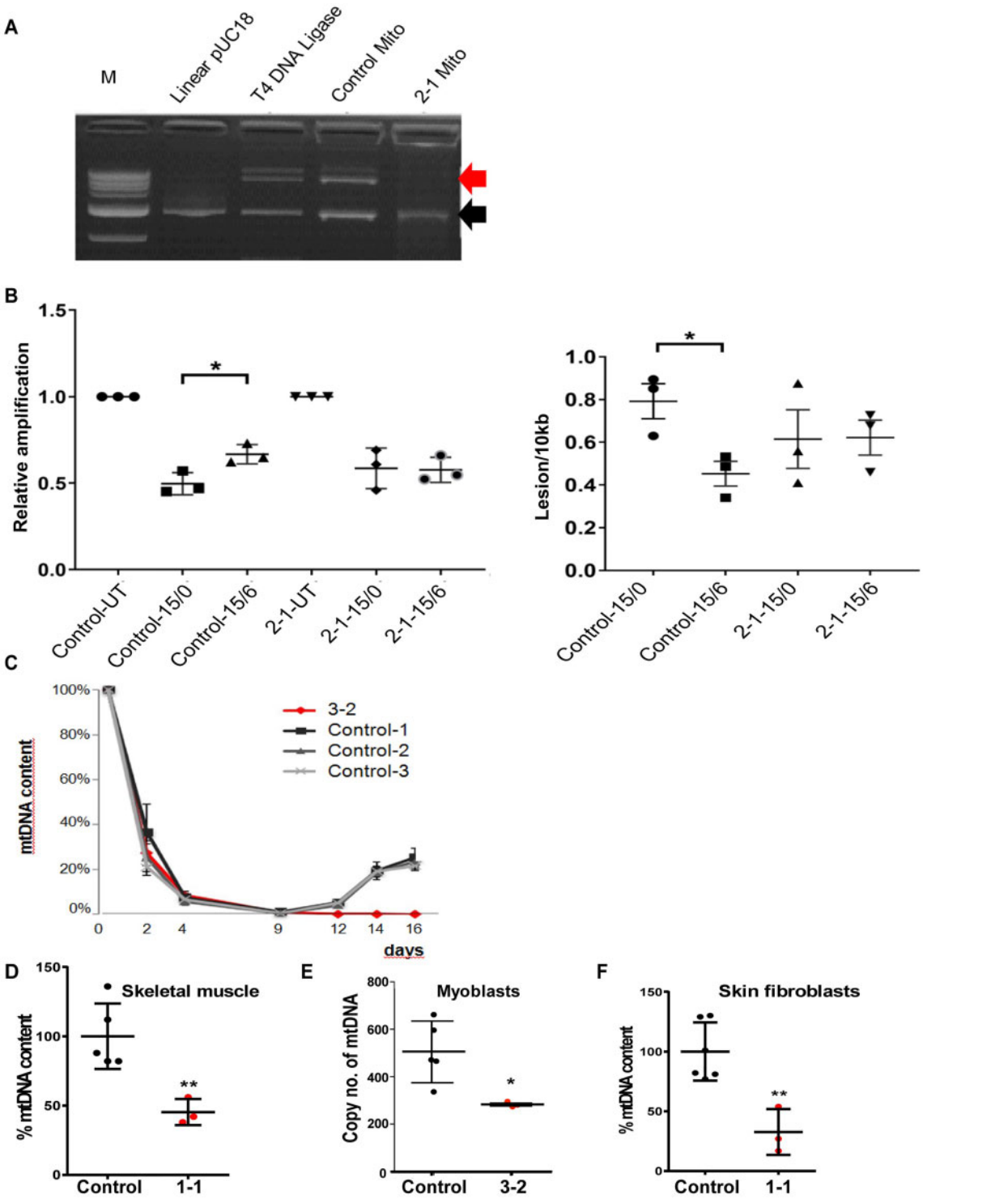

Figure 3 Defects in mtDNA maintenance due to *LIG3* mutations. (**A**) Comparison of ligase activity on linearized pUC18 plasmid DNA (length ~2.6 kb) in mitochondrial extracts between Patient 2-1 and control fibroblasts. T4 DNA ligase = positive control. Black arrow = linearized plasmid; red arrow = expected ligated product. M = molecular weight marker. (**B**) Reduced mtDNA repair kinetics after oxidative damage in control and Patient 2-1-derived fibroblasts. Values were normalized to mtDNA copy number ($n = 3$ experiments). UT = untreated; 15/0 = cells treated for 15 min with H_2O_2 and directly analysed for mtDNA repair kinetics; 15/6 = cells treated 15 min with H_2O_2, recovered for 6 h, then analysed for PCR amplification of a long mtDNA fragment relative to a short PCR fragment (*left*) and the calculated number of lesions per 10 kb of mitochondrial genome (*right*). *$P < 0.05$, ANOVA multiple testing. (**C**) Mitochondrial DNA depletion experiments. Control and Patient 3-2-derived fibroblasts were treated with EtBr for 9 days ($n = 3$ experiments; mean ± standard deviation, SD). (**D**) Quantification of mtDNA in the skeletal muscle of Patient 1-1 (red circles) and controls (black circles). Data shown for $n = 5$ controls and three replicates of the Patient 1-1 muscle biopsy. **$P < 0.01$, Student's *t*-test. (**E**) Mitochondrial DNA quantification in myoblasts from Patient 3-2 (in red; three replicates of Patient 3-2 samples) and controls (in black; data shown for five controls). *$P < 0.05$, Student *t*-test. (**F**) Quantification of mtDNA in skin-derived fibroblasts (Patient 1-1); data shown for five samples for control (black circles) and Patient's 1-1 (red circles). **$P < 0.01$, Student's *t*-test.

replication, in addition to the previously shown impairment in mtDNA repair (Fig. 3C).

We subsequently investigated whether the *LIG3* defects also resulted in reduced mtDNA content. Quantitative assessment of mtDNA copy number in a skeletal muscle biopsy sample from Patient 1-1 demonstrated significant mtDNA depletion compared with controls ($P < 0.01$; Fig. 3D). In Patient 2-2, mtDNA content of the skeletal muscle biopsy was 66% of that in age-matched healthy controls (Supplementary Fig. 4A).[16] A significant decrease in mtDNA copy number was also observed in myoblasts derived from Patient 3-2 compared to controls ($P < 0.05$; Fig. 3E).

Patient 1-1-derived fibroblasts showed significant mtDNA depletion compared to controls ($P < 0.01$; Fig. 3F). Conversely, in skin-derived fibroblasts of Patient 3-2 mtDNA copy number was similar to control cells (Supplementary Fig. 4B).

A quantitative assessment of mtDNA deletions was performed as reported in the Supplementary material, but deletions were not detected in both fibroblasts and skeletal muscle of Patient 1-1 (Supplementary Fig. 4C and D).

Mitochondrial dysfunction caused by *LIG3* mutations

We next investigated how partial mtDNA depletion affected mitochondrial shape and function. Mitochondria were visualized with MitoTracker Green and analysed using confocal fluorescence microscopy. Overall, the mitochondria of mutant fibroblasts (Patient 1-1) displayed a fragmented network compared with control cells (Fig. 4A and Supplementary Fig. 5A–E). Compared to controls, ultrastructural analysis in fibroblasts of Patient 1-1 showed qualitative and quantitative mitochondrial defects such as abnormal cristae and swollen mitochondria and a greater average mitochondrial area (0.011854 versus 0.00644 μm^2, respectively) (Supplementary Fig. 5F).

Analysis of the respiration rate confirmed the mitochondrial dysfunction in patient cells. We observed a significantly decreased uncoupled oxygen consumption (Fig. 4B) and lower ATP content (Fig. 4C) in Patient 1-1 fibroblasts. In addition, USCs which have high mitochondrial content,[32] were established from Patient 3-2 and tested for oxygen consumption rate. The results showed a decrease in oxygen consumption rate in USCs of Patient 3-2 compared with control USCs (Supplementary Fig. 5G). Although no differences in mitochondrial membrane potential were detected in intact control and Patient 1-1 fibroblasts (Supplementary Fig. 5H), in digitonin-permeabilized cells *LIG3*-mutant fibroblasts were less responsive to different respiratory substrates (glutamate malate, ADP, and succinate), inhibitors (oligomycin A and rotenone) and uncoupler (FCCP) compared to controls ($P = 0.0012$; Fig. 4D). MitoSOX™ Red staining (a selective probe for mitochondrial superoxide) detected a significantly increased production of mitochondrial reactive oxygen species in mutant cells compared to control cells ($P = 0.0393$; Fig. 4E), confirming the mitochondrial dysfunction.[33]

As the addition of glutamine (6 mM) has been shown to increase the survival of cells carrying mitochondrial defects, but not control cells,[34] the glutamine concentration was increased in the culture medium from the standard 2 mM to 6 mM. In control fibroblasts a higher glutamine concentration resulted in a decreased growth rate (Supplementary Table 3), in agreement with previous findings,[34–36] indicating that in the absence of mitochondrial defects, excess glutamine may exert a detrimental effect. Conversely, fibroblasts from Patient 1-1 grew more efficiently when exposed to 6 mM than 2 mM glutamine (Fig. 4F and Supplementary Table 3; $P = 0.0248$ at 96 h culture).

In vivo modelling of *LIG3* mutations

As a final line of evidence that the *LIG3* mutations can indeed cause the phenotype observed in the patients, we investigated the intestinal and neuronal phenotypes in a zebrafish model. We evaluated the consequences of *LIG3* mutations on the cerebellar structure[25,37] and the developing digestive system.[38] Reciprocal BLAST with the human LIG3 protein sequence against the zebrafish genome (Zfin v.10) identified a single *lig3* orthologue on chromosome 5, encoding a single transcript for which the encoded protein (NP_001025345) had 69.7% identity to human LIG3 (NP_039269).

We engineered F0 mutants using CRISPR/Cas9 genome editing (Supplementary Fig. 6A and B). F0 clutches with a *lig3* gene disruption (at 3 dpf) showed a significant decrease in the overall cerebellar area compared with both uninjected embryos and embryos injected with gRNA alone (Fig. 5A and B). The observed cerebellar phenotype was consistent with published data from *Lig3*$^{-/-}$ mice.[2]

We also applied a splice-blocking MO antisense oligonucleotide targeting the splice donor site of *lig3* exon 11 (e11i11; Supplementary Fig. 6A). The MO resulted in the skipping of exon 11 and the induction of a frameshift soon thereafter (Supplementary Fig. 6C). Injection of this MO resulted in a dose-dependent decrease in cerebellar area phenocopying the F0 CRISPR mutants ($P < 0.0001$; Supplementary Fig. 7A and B). The cerebellar phenotype was rescued by co-injecting human wild-type *LIG3* mRNA (Supplementary Fig. 7B), but not by mRNA harbouring patient-derived mutant variants (p.K537N and p.G964R) ($P < 0.0001$; Fig. 5C).

We also tested whether *lig3* suppression (MO) or ablation (CRISPR) perturbed the morphology of the gut and the function of the gastrointestinal tract. Quantification of HuC/D-positive neurons showed no significant differences between MO-treated or F0 mutant zebrafish compared with controls (Supplementary Fig. 7C and D). Anti-phosphomyosin staining in the zebrafish gut (8 dpf) did not show any myopathic changes (Supplementary Fig. 7E). We assayed gastrointestinal function at 8 dpf (at which age the gastrointestinal system is developed) by analysing the pattern of peristalsis using high-speed video microscopy. Qualitative scoring by investigators blind to the injection cocktail showed a significant number of morphants and knockout zebrafish with abnormal gut peristalsis [Fig. 5D, Supplementary Videos 1 and 2 (normal versus abnormal peristalsis) and Supplementary Fig. 7F].

Haematoxylin and eosin staining in the zebrafish gut (8 dpf) showed a reduction of goblet cells in morphants (e11i11) and F0 CRISPR mutants compared with controls (Supplementary Fig. 8A and B, $P < 0.01$ and $P < 0.05$, respectively). We then assayed swim bladder formation at 4 dpf (at which age the swim bladder is fully formed) by quantifying the swim bladder area, in morphants and F0 CRISPR mutants. Swim bladder area was reduced in morphants and F0 CRISPR mutants compared with controls (Supplementary Fig. 9A and B, $P < 0.0001$). Next, we quantified the expression of mitochondrial markers (*mt-nd1*, *mt-co1*) in zebrafish embryos at 4dpf. We observed a significant reduction for *mt-nd1* in morphants (e11i11) ($P < 0.01$; Supplementary Fig. 9C) with a similar trend in F0 CRISPR mutants, and a significant reduction for *mt-co1* in morphants (e11i11) ($P < 0.05$; Supplementary Fig. 9C) and F0 CRISPR mutants ($P < 0.05$; Supplementary Fig. 9C). We also tested whether *lig3* suppression (MO) or ablation (CRISPR) perturbed the morphology of the eye. Haematoxylin and eosin staining in the zebrafish eye (5 dpf), revealed a significant reduction of the outer nuclear layer in morphants (e11i11) and F0 CRISPR mutants, compared with controls (Supplementary Fig. 10A and B; $P < 0.0001$).

Discussion

In this study we described a novel recessive syndrome caused by mutations in the *LIG3* gene. The affected individuals in three independent families showed neurogastrointestinal encephalomyopathy characterized by CIPO, neurogenic bladder, myopathic changes, and neurological impairment with stroke-like episodes,

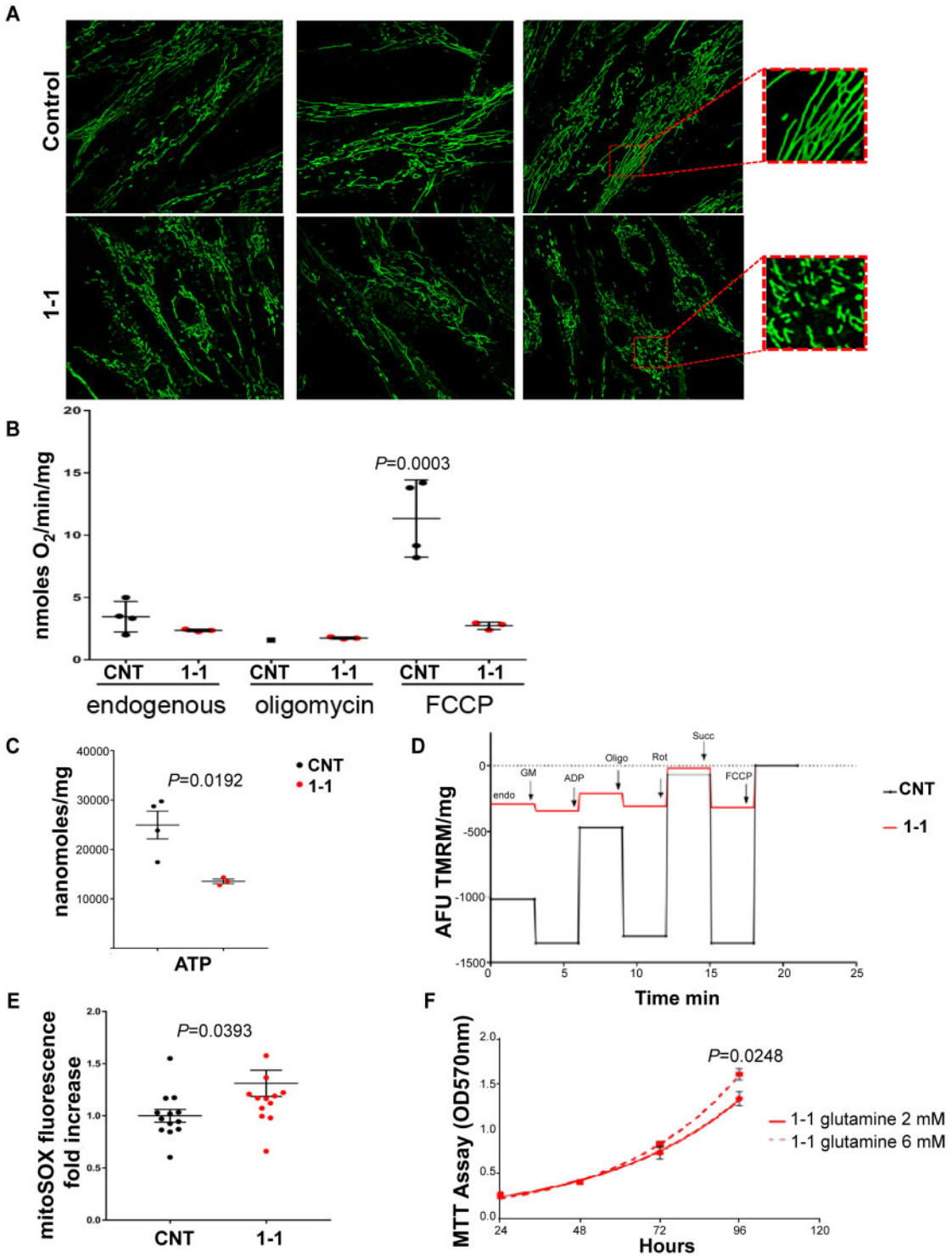

Figure 4 Functional impairment of mitochondria caused by *LIG3* mutations. (**A**) MitoTracker Green staining demonstrated a fragmented mitochondrial network in Patient 1-1 compared to control fibroblasts. Squares on the right are magnified images of the *insets*. (**B**) Mitochondrial oxygen consumption in endogenous and uncoupled conditions. Compared to control (CNT, black circles) cells, fibroblasts from Patient 1-1 (red circles) showed a significantly reduced respiration in the presence of FCCP ($P = 0.0003$; $n = 3$ independent experiments; ANOVA for multiple comparisons). (**C**) ATP content, normalized for protein content, was significantly decreased in patient fibroblasts (red circles) compared with control fibroblasts (black circles; $P = 0.0192$; $n = 3$ independent experiments; Student's *t*-test). (**D**) Analysis of mitochondrial membrane potential in digitonin-permeabilized cells. A representative trace (spectrofluorimetric acquisition) of the pattern measured by the sequential addition of specific substrates (ADP = adenosine diphosphate; GM = glutamate-malate; Succ = succinate), inhibitors (Oligo = oligomycin A; Rot = rotenone) and an uncoupler (FCCP) as indicated. Compared to controls (black line), fibroblasts from Patient 1-1 (red line) were less responsive to different respiratory substrates and inhibitors ($P = 0.0012$; $n = 2$ independent experiments; Student's *t*-test). AFU = arbitrary fluorescence units. (**E**) Analysis of mitochondrial reactive oxygen species production with MitoSOX shows a significant increase in Patient 1-1 fibroblasts (red circles) compared with control fibroblasts (black circles; $P = 0.0393$; Student's *t*-test). (**F**) Growth curve (MTT assay) of Patient 1-1-derived fibroblasts grown in 2 mM (solid line) or 6 mM glutamine (dashed line). Patient cells cultured in 6 mM glutamine show a significantly increased growth after 96 h compared with cells grown in 2 mM glutamine ($P = 0.0248$; ANOVA test; five replicates/each time point).

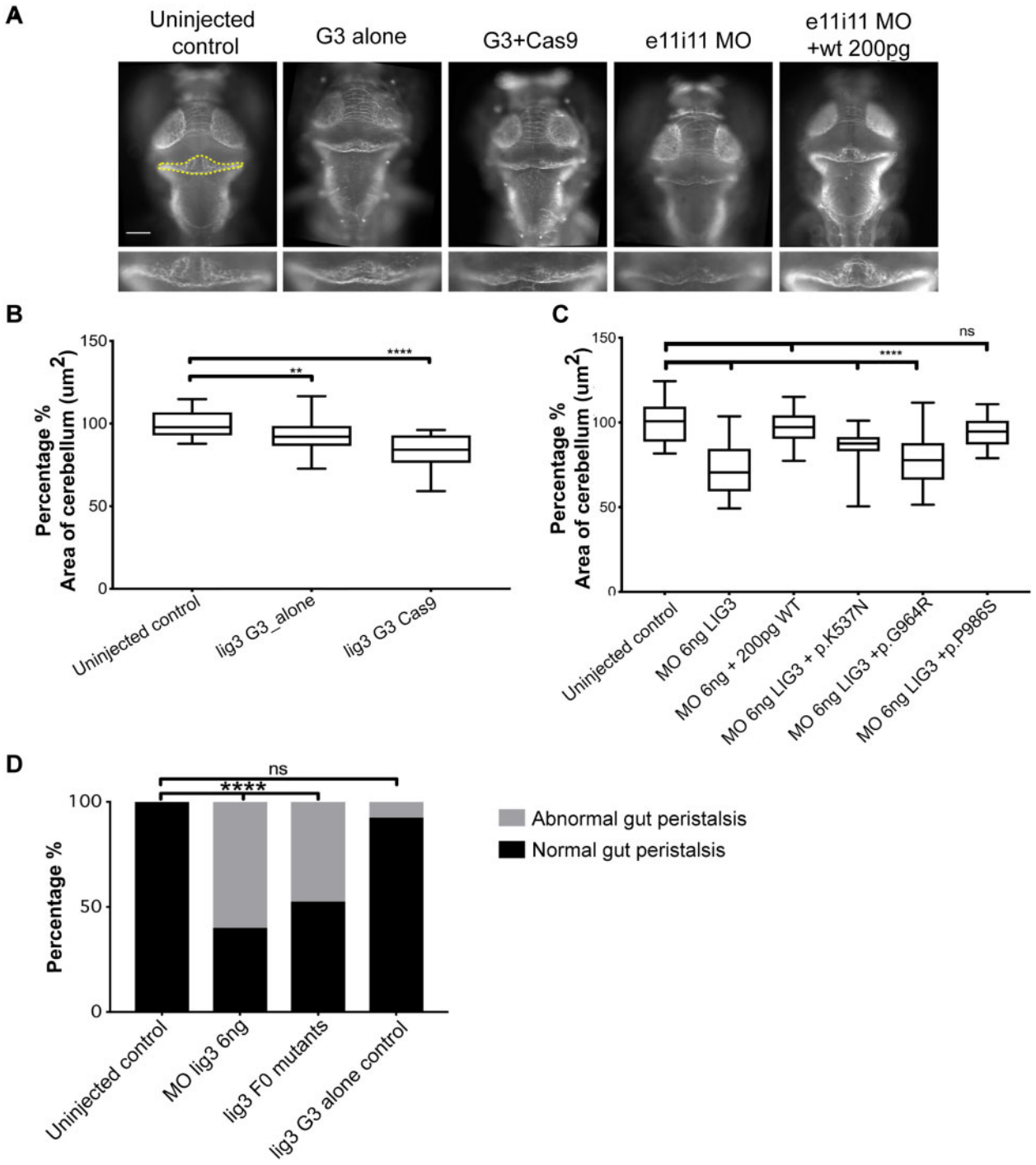

Figure 5 Suppression of *lig3* causes cerebellar hypoplasia and intestinal pseudo-obstruction in the zebrafish. (**A**) Representative dorsal images of larvae (3 dpf) immunostained for acetylated tubulin. To quantify neurons in the cerebellar area, whole-mount acetylated tubulin immunostaining was performed. Cerebellar structures of interest were measured using ImageJ software. Total cerebellar area was measured on acetylated tubulin-stained larvae by outlining structures with a fluorescent signal. Disruption of *lig3* causes cerebellar defects in both F0 CRISPR/Cas9-mutated (G3 + Cas9) zebrafish and morphants (e11i11 MO); e11i11 MO + 200 pg: complementation of *lig3* MO (e11i11 MO) with wild-type (WT) human *LIG3* mRNA (200 pg). Statistical analyses were performed using a nonparametric one-way ANOVA, with the Tukey multiple comparison test. ns = not significant; yellow dashed outline = area of the cerebellum that was measured; G3 = guide alone. (**B**) Quantification of cerebellar area in CRISPR/Cas9 genome edited larvae is shown for a guide targeting exon 8 of *lig3*. Comparison of F0 CRISPR/Cas9 clutches (*lig3* G3 Cas9) with either uninjected embryos or embryos injected with gRNA alone, but no enzyme (*lig3* G3_alone), showed a significant decrease in the overall cerebellar area in F0 mutants ($P < 0.0001$ for each comparison, replicated, scored blind). (**C**) Complementation of *lig3* MO with wild-type (WT) or mutated human mRNA. In contrast to embryos injected with wild-type *LIG3* mRNA or with a benign variant, i.e. not affecting ligase activity (p.P986S, rs498673), which were indistinguishable from the uninjected ones, injection with mRNA encoding p.K537N and p.G964R did not show rescue of the cerebellar phenotype. (**D**) Ablation of *lig3* causes abnormal gut peristalsis in F0 CRISPR/Cas9 mutants and morphants ($P < 0.0001$, $n = 40$ larvae/batch, replicated, χ^2 test). $^{*}P < 0.05$; $^{**}P < 0.01$; $^{***}P < 0.001$; $^{****}P < 0.0001$.

epilepsy and leukoencephalopathy. The underlying cause is a defect in mtDNA ligase activity, leading to decreased mtDNA repair capacity, reduced mtDNA content and impaired mitochondrial function.

It was previously reported that the inactivation of *Lig3* led to loss of cell viability and early embryonic lethality in mice, with profound mitochondrial dysfunction due to reduced mtDNA in the nervous system.[2,5] At the single cell level, viability could be restored by mitochondrial targeting of another DNA ligase, showing that the pathogenic effect was caused by the inability to ligate mtDNA. Neuron-targeted conditional *Lig3* knockout mice showed a reduced brain size and cerebellar abnormalities with increased apoptosis in the granular layer, consistent with our observation of the zebrafish phenotype and brain defects as manifested by affected members of Family 3.[5] Gut peristalsis was not investigated in the *Lig3* mutant mice, so we link for the first time this phenotype to *LIG3* mutations. However, this is not unexpected as *POLG* mutations also cause compromised mtDNA maintenance and gut dysmotility.[39,40]

Given the functional redundancy of different ligases in the nucleus, our study suggests that primary mitochondrial dysfunction is the major, if not the only, contributor to the clinical phenotype, as documented by the downstream disruption of mtDNA maintenance and repair, with the depletion of mitochondrial genomes in skeletal muscle and fibroblasts from patients. This explains the impaired mitochondrial function in tissues with high-energy requirements, such as neurons and muscle cells. Disruption of *lig3* in the zebrafish recapitulated the cerebellar phenotype (a hallmark of *Lig3*$^{-/-}$ mice) and eye defects, as well as the severe impairment of gut propulsion that was observed in all patients of the three investigated families. Disruption of *lig3* also led to a significant decrease in the expression of mitochondrial markers in the zebrafish.

The features of our patients are reminiscent of known mitochondrial disorders, such as MNGIE, MELAS, and *POLG*-associated phenotypes, which all involve post-mitotic, high-energy dependent tissues, i.e. brain, skeletal muscle, and smooth muscle.[41] Notably, mtDNA depletion occurs in both MNGIE and *POLG*-mutant patients. The latter patients may additionally show migraine and epilepsy with stroke-like episodes, which are features also observed in MELAS as well as in our *LIG3*-mutant patients. Interestingly, multiple deletions in mtDNA, which are frequently observed in both MNGIE and *POLG*-associated phenotypes, were not found in patients with *LIG3* mutations. The overall CNS involvement in patients with *LIG3* mutations was more severe than in MNGIE patients with *TYMP* mutations, who usually have asymptomatic leukoencephalopathy.

The age of onset of major symptoms in patients with *LIG3* mutations was in infancy for Family 3, paediatric age for Family 1 and adult age for Family 2. The rate of progression of disease also seemed faster in Family 3 and slower in Family 2. We hypothesize that the difference in severity is caused by differences in residual protein levels and activity, but this has not been addressed directly. It is possible that the residual level of mitochondrial ligase function is higher in point mutants disrupting the interaction with XRCC1 (Families 1 and 2), which may lead to decreased protein levels but relatively normal function, whereas the mutations in Family 3 may lead to severely reduced protein levels and function. Further identification of patients with additional *LIG3* mutations will increase our understanding of the phenotypes of this new disorder, as well as provide a comparison with other mitochondrial diseases. Moreover, *LIG3* polymorphisms have been associated with a variety of pathological conditions such as tumours, neurodegenerative disorders (i.e. Alzheimer's disease), recurrent depression and neural tube defects,[42–47] suggesting that a better understanding of LIG3 function may have implication also in these diseases.

There is still a limited understanding of the metabolic consequences of mitochondrial defects.[48,49] Glutamine is crucially involved in metabolic fluxes, by replenishing the intermediates of mitochondrial respiration.[50,51] A recent study showed that increased glutamine concentration improved the survival of cells carrying mtDNA defects.[34] In our study, glutamine added to *LIG3*-mutant fibroblasts led to an increase in cell growth. These results suggest that the bioenergetic impairment induced by *LIG3* mutations may be ameliorated by boosting the glutamine anaplerotic pathway although the evidence is still limited.[34]

In conclusion, we described a new mitochondrial recessive disorder caused by biallelic variants in *LIG3*, with a clinical phenotype characterized by CIPO and neurologic abnormalities, including brain abnormalities similar to those observed in other mitochondrial diseases, epilepsy and stroke-like episodes, which are clearly associated with mitochondrial dysfunction caused by defective mtDNA maintenance.

Web resources

CHOPCHOP: https://chopchop.rc.fas.harvard.edu/
ClustalOmega: https://www.ebi.ac.uk/Tools/msa/clustalo/
The Single Nucleotide Polymorphism Database (dbSNP): https://www.ncbi.nlm.nih.gov/snp
Genome Aggregation database (gnomAD): http://gnomad.broadinstitute.org/
GraphPad Prism: https://www.graphpad.com/scientific-software/prism/
Genotype-Tissue Expression (GTEx): https://commonfund.nih.gov/gtex
Human Splicing Finder (HSF) v.3.1: http://www.umd.be/HSF3/index.html
The Human Protein Atlas: https://www.proteinatlas.org/
ImageJ (National Institutes of Health, Bethesda, MD): http://rsbweb.nih.gov/ij
Mendelian Clinically Applicable Pathogenicity Score (M-CAP): http://bejerano.stanford.edu/mcap/
Pfam database: https://pfam.xfam.org/
Prediction of functional effects of human nsSNPs (PolyPhen-2): http://genetics.bwh.harvard.edu/pph2/
Primer3: http://bioinfo.ut.ee/primer3/
Protein Data Bank (PDB): http://www.rcsb.org/
Protein Variation Effect Analyzer (Provean): http://provean.jcvi.org/index.php
Zebrafish Information Network (ZFIN): https://zfin.org/

Acknowledgements

We greatly appreciate the cooperation of the patients and their families who participated in the study. We thank A. Astolfi for technical help in NGS, F.M. Santorelli and D. Cassandrini for clinical evaluation of muscle biopsies, G. La Marca for performing the thymidine phosphorylase assay using patient-derived urine. We thank A. Kita, A. Hosoya, M. Kawai, M. Kusunoki, M. Tachikawa and J. Odijk for technical assistance. We also thank H. Inagaki, S. Minamikawa, H. Nagase, M. Nishiyama, H. Awano, Y. Aoki, T. Kawada, M. Matsumoto, N. Matsumoto and N. Taniguchi for their technical support and valuable comments.

Funding

This work was supported by Telethon Grant GGP15171 to E.B. and R.D.G. and by a donation from Kobe city to the Department of General Pediatrics, Kobe University Graduate School of Medicine (K550003302). S.C. was supported by a Dutch Cancer Foundation

grant (KWF11011). V.C. and A.M. were supported by the Italian Ministry of Health ("Ricerca Corrente" funding). R.D.G. is the recipient of grants from University of Ferrara (FAR and FIR funds).

Competing interests

The authors report no competing interests.

Supplementary material

Supplementary material is available at *Brain* online.

References

1. Cuneo MJ, Gabel SA, Krahn JM, Ricker MA, London RE. The structural basis for partitioning of the XRCC1/DNA ligase 3-α BRCT-mediated dimer complexes. *Nucleic Acids Res*. 2011;39:7816-7827.
2. Gao Y, Katyal S, Lee Y, et al. DNA ligase 3 is critical for mtDNA integrity but not Xrcc1-mediated nuclear DNA repair. *Nature*. 2011;471:240-244.
3. Odell ID, Barbour JE, Murphy DL, et al. Nucleosome disruption by DNA ligase 3-XRCC1 promotes efficient base excision repair. *Mol Cell Biol*. 2011;31:4623-4632.
4. Shokolenko IN, Fayzulin RZ, Katyal S, McKinnon PJ, Wilson GL, Alexeyev MF. Mitochondrial DNA ligase is dispensable for the viability of cultured cells but essential for mtDNA maintenance. *J Biol Chem*. 2013;288:26594-26605.
5. Simsek D, Furda A, Gao Y, et al. Crucial role for DNA ligase 3 in mitochondria but not in Xrcc1-dependent repair. *Nature*. 2011; 471:245-258.
6. DiMauro S, Schon EA, Carelli V, Hirano M. The clinical maze of mitochondrial neurology. [Review]. *Nat Rev Neurol*. 2013;9: 429-444.
7. Akbari M, Keijzers G, Maynard S, et al. Overexpression of DNA ligase 3 in mitochondria protects cells against oxidative stress and improves mitochondrial DNA base excision repair. *DNA Repair (Amst)*. 2014;16:44-53.
8. Di Nardo G, Di Lorenzo C, Lauro A, et al. Chronic intestinal pseudo-obstruction in children and adults: diagnosis and therapeutic options [Review]. *Neurogastroenterol Motil*. 2017; e12945.
9. Downes TJ, Cheruvu MS, Karunaratne TB, De Giorgio R, Farmer AD. Pathophysiology, diagnosis, and management of chronic intestinal pseudo-obstruction [Review]. *J Clin Gastroenterol*. 2018; 52:477-489.
10. Goldstein AM, Thapar N, Karunaratne TB, De Giorgio R. Clinical aspects of neurointestinal disease: pathophysiology, diagnosis, and treatment [Review]. *Dev Biol*. 2016;417:217-228.
11. Nishino I, Spinazzola A, Hirano M. Thymidine phosphorylase gene mutations in MNGIE, a human mitochondrial disorder. *Science*. 1999;283:689-692.
12. Carelli V, La Morgia C. Clinical syndromes associated with mtDNA mutations: where we stand after 30 years [Review]. *Essays Biochem*. 2018;62:235-254.
13. Lakshmipathy U, Campbell C. The human DNA ligase 3 gene encodes nuclear and mitochondrial proteins. *Mol Cell Biol*. 1999; 19:3869-3876.
14. Tomkinson AE, Sallmyr A. Structure and function of the DNA ligases encoded by the mammalian LIG3 gene. *Gene*. 2013;531: 150-157.
15. Giordano C, Iommarini L, Giordano L, et al. Efficient mitochondrial biogenesis drives incomplete penetrance in Leber's hereditary optic neuropathy. *Brain*. 2014;137:335-353.
16. Dimmock D, Tang LY, Schmitt ES, Wong LJ. Quantitative evaluation of the mitochondrial DNA depletion syndrome. *Clin Chem*. 2010;56:1119-1127.
17. Furda A, Santos JH, Meyer JN, Van Houten B. Quantitative PCR-based measurement of nuclear and mitochondrial DNA damage and repair in mammalian cells. *Methods Mol Biol*. 2014; 1105:419-437.
18. Kornblum C, Nicholls TJ, Haack TB, et al. Loss-of-function mutations in MGME1 impair mtDNA replication and cause multisystemic mitochondrial disease. *Nat Genet*. 2013;45: 214-219.
19. Lakshmipathy U, Campbell C. Double strand break rejoining by mammalian mitochondrial extracts. *Nucleic Acids Res*. 1999;27: 1198-1204.
20. Diquigiovanni C, Bergamini C, Evangelisti C, et al. Mutant MYO1F alters the mitochondrial network and induces tumor proliferation in thyroid cancer. *Int J Cancer*. 2018;143: 1706-1719.
21. Bergamini C, Moruzzi N, Sblendido A, Lenaz G, Fato R. A water soluble CoQ_{10} formulation improves intracellular distribution and promotes mitochondrial respiration in cultured cells. *PLoS One*. 2012;7:e33712.
22. Niederriter AR, Davis EE, Golzio C, Oh EC, Tsai IC, Katsanis N. In vivo modeling of the morbid human genome using Danio rerio. *J Vis Exp*. 2013;24:e50338.
23. Marjoram L, Alvers A, Deerhake ME, et al. Epigenetic control of intestinal barrier function and inflammation in zebrafish. *Proc Natl Acad Sci USA*. 2015;112:2770-2775.
24. Sanna-Cherchi S, Khan K, Westland R, et al. Exome-wide Association Study Identifies GREB1L mutations in congenital kidney malformations. *Am J Hum Genet*. 2017;101:789-802.
25. Loviglio MN, Arbogast T, Jønch AE, et al. The Iimmune signaling adaptor LAT contributes to the neuroanatomical phenotype of 16p11-2 BP2-BP3 CNVs. *Am J Hum Genet*. 2017;101:564-577.
26. Ohkubo H, Iida H, Takahashi H, et al. An epidemiologic survey of chronic intestinal pseudo-obstruction and evaluation of the newly proposed diagnostic criteria. *Digestion*. 2012;86:12-19.
27. Canafoglia L, Franceschetti S, Antozzi C, et al. Epileptic phenotypes associated with mitochondrial disorders. *Neurology*. 2001; 56:1340-1346.
28. El-Gebali S, Mistry J, Bateman A, et al. The Pfam protein families database in 2019. *Nucleic Acids Res*. 2019;47:D427-D432.
29. Madeira F, Park YM, Lee J, et al. The EMBL-EBI search and sequence analysis tools APIs in 2019. *Nucleic Acids Res*. 2019;47: W636-W641.
30. Calabrese R, Capriotti E, Fariselli P, Martelli PL, Casadio R. Functional annotations improve the predictive score of human disease-related mutations in proteins. *Hum Mutat*. 2009;30: 1237-1244.
31. Savojardo C, Fariselli P, Martelli PL, Casadio R. INPS-MD: a web server to predict stability of protein variants from sequence and structure. *Bioinformatics*. 2016;32:2542-2544.
32. Lazzeri E, Ronconi E, Angelotti ML, et al. Human urine-derived renal progenitors for personalized modeling of genetic kidney disorders. *JASN*. 2015;26:1961-1974.
33. Diquigiovanni C, Bergamini C, Diaz R, et al. A novel mutation in SPART gene causes a severe neurodevelopmental delay due to mitochondrial dysfunction with complex I impairments and altered pyruvate metabolism. *FASEB J*. 2019;33:11284-11302.
34. Chen Q, Kirk K, Shurubor YI, et al. Rewiring of glutamine metabolism is a bioenergetic adaptation of human cells with mitochondrial DNA mutations. *Cell Metab*. 2018;27:1007-1025.
35. Pichili VB, Rao KV, Jayakumar AR, Norenberg MD. Inhibition of glutamine transport into mitochondria protects astrocytes from ammonia toxicity. *Glia*. 2007;55:801-809.

36. Rama Rao KV, Jayakumar AR, Norenberg MD. Induction of the mitochondrial permeability transition in cultured astrocytes by glutamine. *Neurochem Int*. 2003;43:517-523.
37. Guissart C, Latypova X, Rollier P, et al. Dual Molecular Effects of dominant RORA mutations cause two variants of syndromic intellectual disability with either autism or cerebellar ataxia. *Am J Hum Genet*. 2018;102:744-759.
38. Bonora E, Bianco F, Cordeddu L, et al. Mutations in RAD21 disrupt regulation of APOB in patients with chronic intestinal pseudo-obstruction. *Gastroenterology*. 2015;148:771-782.
39. Filosto M, Mancuso M, Nishigaki Y, et al. Clinical and genetic heterogeneity in progressive external ophthalmoplegia due to mutations in polymerase gamma. *Arch Neurol*. 2003;60:1279-1284.
40. Van Goethem G, Schwartz M, Löfgren A, Dermaut B, Van Broeckhoven C, Vissing J. Novel *POLG* mutations in progressive external ophthalmoplegia mimicking mitochondrial neurogastrointestinal encephalomyopathy. *Eur J Hum Genet*. 2003;11:547-549.
41. Kanungo S, Morton J, Neelakantan M, Ching K, Saeedian J, Goldstein A. Mitochondrial disorders. [Review]. *Ann Transl Med*. 2018;6:475.
42. Corral R, Lewinger JP, Joshi AD, et al. Genetic variation in the base excision repair pathway, environmental risk factors, and colorectal adenoma risk. *PLoS One*. 2013;8:e71211.
43. Czarny P, Kwiatkowski D, Toma M, et al. Impact of single nucleotide polymorphisms of base excision repair genes on DNA damage and efficiency of DNA repair in recurrent depression disorder. *Mol Neurobiol*. 2017;54:4150-4159.
44. Kwiatkowski D, Czarny P, Toma M, et al. Association between single-nucleotide polymorphisms of the *hOGG1, NEIL1, APEX1, FEN1, LIG1*, and *LIG3* genes and Alzheimer's disease risk. *Neuropsychobiology*. 2016;73:98-107.
45. Li D, Suzuki H, Liu B, et al. DNA repair gene polymorphisms and risk of pancreatic cancer. *Clin Cancer Res*. 2009;15:740-746.
46. Li G, Wang X, Wang X, et al. Polymorphism rs1052536 in base excision repair gene is a risk factor in a high-risk area of neural tube defects in China. *Med Sci Monit*. 2018;24:5015-5026.
47. Liao YH, Ren JT, Zhang W, et al. Polymorphisms in homologous recombination repair genes and the risk and survival of breast cancer. *Gene Med*. 2017;19:9-10.
48. Eales KL, Hollinshead KE, Tennant DA. Hypoxia and metabolic adaptation of cancer cells. [Review]. *Oncogenesis*. 2016;5:e190.
49. Smeitink JA, Zeviani M, Turnbull DM, Jacobs HT. Mitochondrial medicine: a metabolic perspective on the pathology of oxidative phosphorylation disorders [Review]. *Cell Metab*. 2006;3:9-13.
50. Daye D, Wellen KE. Metabolic reprogramming in cancer: unraveling the role of glutamine in tumorigenesis [Review]. *Semin Cell Dev Biol*. 2012;23:362-369.
51. Sullivan LB, Gui DY, Hosios AM, Bush LN, Freinkman E, Vander Heiden MG. Supporting aspartate biosynthesis is an essential function of respiration in proliferating cells. *Cell*. 2015;162:552-563.